The mantle transition zone beneath the Afar Depression and adjacent regions: implications for mantle plumes and hydration

C.A. Reed, S.S. Gao, K.H. Liu and Y. Yu

Geology and Geophysics Program, Missouri University of Science and Technology, Rolla, MO 65409, USA. E-mail: sgao@mst.edu

SUMMARY
The Afar Depression and its adjacent areas are underlain by an upper mantle marked by some of the world's largest negative velocity anomalies, which are frequently attributed to the thermal influences of a lower-mantle plume. In spite of numerous studies, however, the existence of a plume beneath the area remains enigmatic, partially due to inadequate quantities of broad-band seismic data and the limited vertical resolution at the mantle transition zone (MTZ) depth of the techniques employed by previous investigations. In this study, we use an unprecedented quantity (over 14 500) of *P*-to-*S* receiver functions (RFs) recorded by 139 stations from 12 networks to image the 410 and 660 km discontinuities and map the spatial variation of the thickness of the MTZ. Non-linear stacking of the RFs under a 1-D velocity model shows robust *P*-to-*S* conversions from both discontinuities, and their apparent depths indicate the presence of an upper-mantle low-velocity zone beneath the entire study area. The Afar Depression and the northern Main Ethiopian Rift are characterized by an apparent 40–60 km depression of both MTZ discontinuities and a normal MTZ thickness. The simplest and most probable interpretation of these observations is that the apparent depressions are solely caused by velocity perturbations in the upper mantle and not by deeper processes causing temperature or hydration anomalies within the MTZ. Thickening of the MTZ on the order of 15 km beneath the southern Arabian Plate, southern Red Sea and western Gulf of Aden, which comprise the southward extension of the Afro-Arabian Dome, could reflect long-term hydration of the MTZ. A 20 km thinning of the MTZ beneath the western Ethiopian Plateau is observed and interpreted as evidence for a possible mantle plume stem originating from the lower mantle.

Key words: Continental tectonics: extensional; Hotspots; Large igneous provinces; Africa.

1 INTRODUCTION

Continental flood basalts comprising many terrestrial Large Igneous Provinces (LIPs) are widely considered to be the consequence of the eruption of voluminous decompression-generated melt associated with upwelling mantle plumes (Coffin & Eldholm 1994). A prime example of a continental LIP is the Ethiopian flood basalt province (Fig. 1) which began erupting as early as ∼45 Ma beginning in SW Ethiopia (Ebinger *et al.* 1993; George *et al.* 1998) and continued until roughly 11 Ma (Kieffer *et al.* 2004). These extensive flood basalts are often attributed to the hypothesized Afar plume (Hofmann *et al.* 1997; Furman *et al.* 2006). Kieffer *et al.* (2004) related the origin of the dominant ∼30 Ma phase of flood volcanism to broad regional upwelling of the African Superswell-related low-velocity province, while the shield volcanoes, the oldest of which overlies younger flood basalts at ∼13°N atop the Western Plateau in NW Ethiopia, were attributed to the influence of plume-related interactions.

A pertinent question to proffer, then, is whether the recent Ethiopian–Afar LIP overlies a present-day mantle plume structure. Plumes, as a result of the entrainment of lower-mantle low-viscosity material, are popularly thought to adopt a bulbous head structure with a stem trailing from a source region in the lowermost mantle (e.g. Montelli *et al.* 2004), and are likely characterized by longevities exceeding hundreds of millions of years (Jellinek & Manga 2004; Dannberg & Sobolev 2015). Such a longevity has been similarly hypothesized by Furman *et al.* (2006) for the Afar plume. It is unknown whether this longevity should imply the persistence of a plume stem within the mantle transition zone (MTZ), especially since the structure of the mantle beneath Ethiopia remains enigmatic in spite of numerous geochemical (e.g. Hofmann *et al.* 1997), geodynamic (e.g. Behn *et al.* 2004) and seismological (e.g. Montelli *et al.* 2004; Civiero *et al.* 2015) investigations.

1.1 Previous investigations of mantle velocity structure beneath Afar

Geochemical sampling and petrogenetic modeling have suggested that the sub-Ethiopian upper mantle is hotter-than-normal, which may imply the generation of melt as a consequence of the
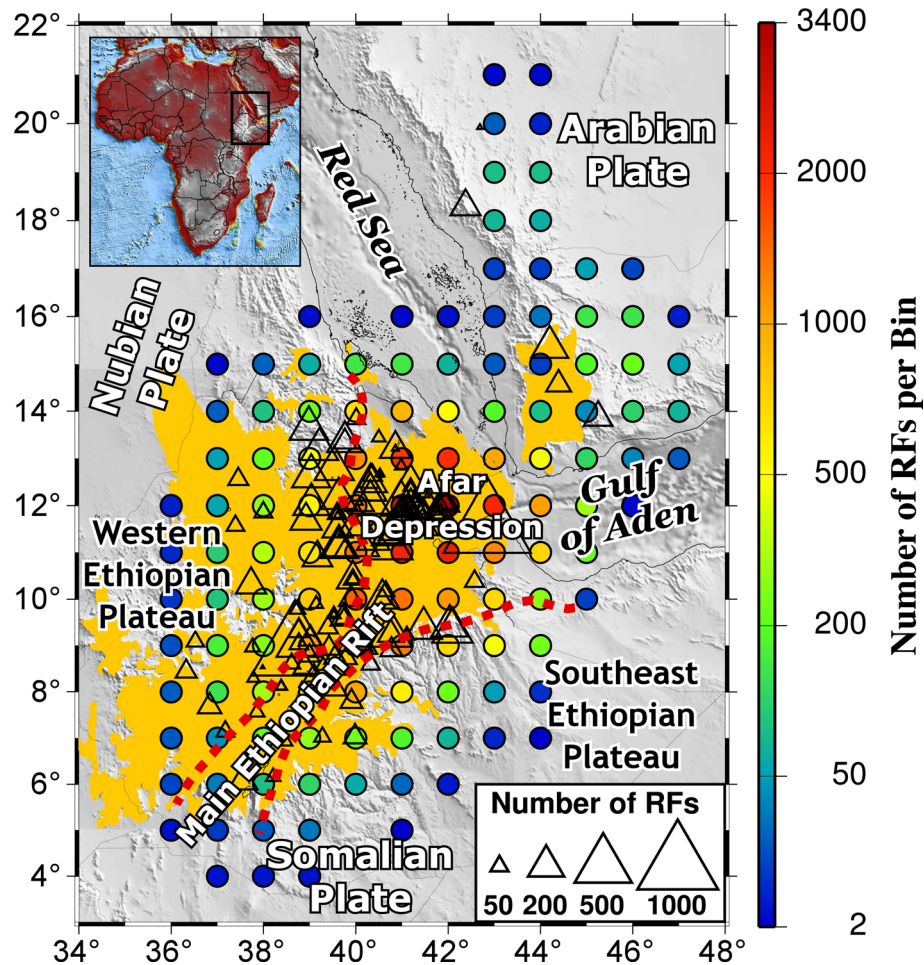
Figure 1. Basemap demonstrating the number of receiver functions in fixed radius = 1° bins, locations of stations used in this study (triangles) and Miocene border faults encompassing the Afar Depression and the Main Ethopian Rift (red dashed lines). The orange infilled region is the surficial extent of the Ethiopian flood basalt province (Coffin & Eldholm 1994). The circumscribed triangle diameter is directly proportional to the number of high-quality RFs recorded by the corresponding station. The quadrangle in the inset of Africa represents the study region of this analysis.

continued ascending of deep-mantle plume material (Rooney *et al.* 2012; Ferguson *et al.* 2013). On the other hand, Rychert *et al.* (2012) employed seismic *Sp* receiver functions (RFs) coupled with geodynamic modeling to argue for decompression melting in the absence of a significant plume influence beneath the Afar rift zone. Global finite-frequency tomography conducted by Montelli *et al.* (2004) revealed a plume approximately 400 km in diameter extending into the lower mantle beneath the Afar Depression, while Hansen & Nyblade (2013) imaged focused upper mantle low δV_p anomalies of −3 per cent centred beneath the Main Ethiopian Rift (MER). Benoit *et al.* (2006) imaged sub-Ethiopian *P*- and *S*-wave velocity perturbations between 150 and 400 km as low as −2.5 and −4.0 per cent, respectively, while a later study conducted by Bastow *et al.* (2008) revealed smaller relative δV_p values of −1.5 per cent beneath Afar, though they estimated that values of *P*-wave velocity perturbation on the order of −6 per cent are required to match their observed delay times. Hammond *et al.* (2013) obtained similar values using additional data and observed a reduction in velocity anomalies beyond 200 km depth. A recent study conducted by Thompson *et al.* (2015) found persistent low *S*-wave velocities on the order of −2 per cent beneath the northern MER and Afar Depression, while localized low-velocity anomalies found below 410 km were confined only beneath the northern MER and the Red Sea-Gulf of Aden junction. Their results show normal seismic velocities at the 660 km discon-

tinuity beneath the majority of the Afar Depression and normal to fast *S*-anomalies beneath the Western Plateau. In addition, Civiero *et al.* (2015) employed *P*-wave traveltime tomography to provide velocity anomaly estimates suggesting the presence of two 100–200 km diameter upwellings, comprised of material consisting of a 100±50 K temperature anomaly, originating from below 700 km and extending into the upper mantle beneath the Afar Depression and the western flank of the MER. The inconsistency among these techniques in terms of providing a definitive answer to the existence of one or more plumes in the Afar area is probably due to intrinsic limitations on the vertical resolution of teleseismic body-wave tomography and a lack of adequate quantities of high-quality data.

1.2 Topography of MTZ discontinuities and geodynamic implications

Confining the topographic variations of the MTZ discontinuities offers an alternative estimate of mantle thermal structure. The MTZ separates the upper and lower mantle through a pair of abrupt seismic discontinuities at about 410 and 660 km (*d*410 and *d*660) resulting from olivine-wadsleyite and ringwoodite-perovskite phase transitions, respectively (Fig. 2; Ringwood 1975). A positive (negative) thermal anomaly perturbing the entirety of the MTZ will result in an overall thinning (thickening) as a consequence of exothermic
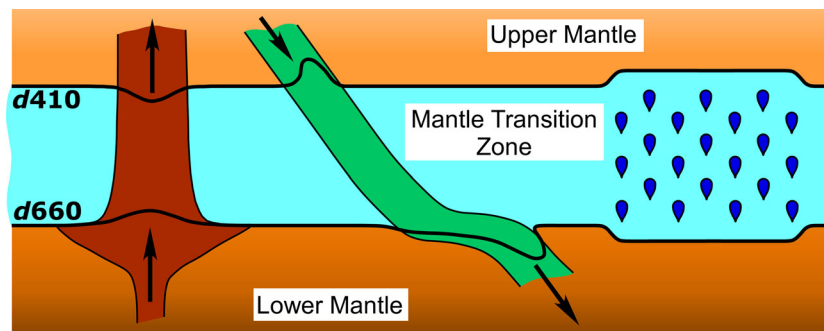
Figure 2. Schematic environmental representations of MTZ thinning under the influence of a mantle plume (left), thickening due to subduction of a cold slab (centre) and thickening due to a relative increase in overall MTZ hydration content (right).

and endothermic phase transitions across the *d*410 and *d*660, respectively (Bina & Helffrich 1994). For instance, respective Clapeyron slopes of +2.9 and −2.1 MPa K^{-1} for the *d*410 and *d*660 (Bina & Helffrich 1994) will induce a depression of 20 km along the former under the influence of a ∼240 K rise in temperature across the *d*410, while an uplift of the same along the *d*660 would require a rise in temperature upwards of 340 K. It is worth noting, however, that a range of values for the Clapeyron slope exist for both the *d*410 (1.5–3.0 MPa K^{-1}) and *d*660 (−4.0 to −2.0 MPa K^{-1}) and thus predicting the thermal behaviour within the MTZ is subject to considerable interpretation (see Tauzin & Ricard 2014 for values and references therein). The interpretation of MTZ discontinuity depth observations is further complicated by the fact that under high-temperature (exceeding 1800 °C) conditions, the phase transition represented by the *d*660 is dominated by the transition from majorite garnet to perovskite, which has a positive Clapeyron slope of +1.3 MPa K^{-1} (Hirose 2002).

Mounting evidence from tomographic and petrophysical studies also suggests that the MTZ functions as the primary mantle reservoir of water (Ohtani *et al.* 2004), wherein storage occurs within wadsleyite and ringwoodite, which may possess water solubilities as high as 3 wt per cent (Bolfan-Casanova *et al.* 2000). Abundant quantities of hydrous minerals within the MTZ may have the same effect as a decrease in temperature and thus result in a depression of the *d*660 and uplift of the *d*410 (Fig. 2; Litasov *et al.* 2005).

Similar to seismic tomography studies, previous investigations of the MTZ beneath the Afar Depression and adjacent areas have led to conflicting conclusions regarding the existence of the Afar plume. MTZ studies using data recorded by long-running stations ATD (11.53°N, 42.85°E) in the Afar Depression and FURI (8.90°N, 38.68°E) on the Ethiopian Plateau did not discover any significant anomaly in MTZ thickness beneath the northernmost East African rift system (Chevrot *et al.* 1999; Tauzin *et al.* 2008). A prominent thickening of the MTZ corresponding to a southwestward depression of the *d*660 beneath the MER detected by Cornwell *et al.* (2011) was attributed to lateral garnet compositional variations in the lowermost MTZ, and MTZ thinning coincident with a regional 30–40 km depression of the otherwise flat *d*410 beneath Ethiopia was linked to the African Superplume. Nyblade *et al.* (2000), who used data primarily from station ATD, obtained a 244 km MTZ thickness and used it to justify the presence of an entirely upper-mantle anomaly beneath the Afar. Benoit *et al.* (2006) reported a poorly imaged *d*410 and observed a shallow *d*660 beneath Ethiopia, which was subsequently attributed to a broad Superplume-related thermal flux. Most recently, Thompson *et al.* (2015) jointly analysed *S*-wave tomography and *P*-to-*S* RFs beneath the MER and Afar Depression and discovered a first-order positive correlation

between the depths of the *d*410 and *d*660, indicating an absence of thermal activity traversing the MTZ discontinuities. They also proposed the existence of a hydrated MTZ beneath northern Afar based on negative-amplitude pulses above the *d*410 indicative of a melt layer.

In this study, we apply a non-plane wave *P*-to-*S* RF stacking procedure to image the *d*410 and *d*660 (Gao & Liu 2014a) by taking advantage of the recent availability of a greatly expanded data set recorded by 139 stations from 12 networks, including 17 stations that we installed and operated in central Afar (Reed *et al.* 2014) over the period from early 2010 to middle 2011. As demonstrated below, the significantly increased quantity and quality of data resulted in dramatically improved imaging of the *d*410 and *d*660. Consequently, for the first time, this study provides evidence for the possible existence of a plume stem beneath the western Ethiopian Plateau, as well as the presence of MTZ hydration beneath the southern Arabian plate and Gulf of Aden.

2 DATA AND METHODS

Three-component broad-band seismic data were acquired from the Incorporated Research Institutions for Seismology (IRIS) Data Management Center (DMC) for the period spanning mid-1993 to late-2014. The recording stations belong to one of 12 networks which operated throughout the Afar Depression and adjacent regions. A breakdown of the networks, their periods of operation and total data contributions can be found in Table S1, Supporting Information. Parameters used for data selection and processing, including epicentral distance ranges, event magnitude cut-off, filtering frequencies, as well as selection criteria for usable RFs are the same as those in Gao & Liu (2014b) for imaging MTZ discontinuities beneath the contiguous United States. A total of 14 589 high-quality RFs recorded by 139 stations are computed using the procedure of Ammon (1991). In comparison, the number of RFs used by Thompson *et al.* (2015) to image the MTZ beneath the Afar rift and adjacent areas is 5158, that by Cornwell *et al.* (2011) is 1923, that by Benoit *et al.* (2006) is 1275 and that by Nyblade *et al.* (2000) is 306.

We image the *d*410 and *d*660 using the approach outlined in Gao & Liu (2014a). It applies normal moveout corrections under a non-plane wave assumption, which is more accurate and results in sharper *d*410 and *d*660 arrivals than approaches based on the plane wave assumption. The moveout corrected RFs with ray-piercing points (calculated at a depth of 535 km) in circular bins of 1° radius are stacked to form a depth-series for each of the bins. The interval between neighbouring bins is 1 geographic degree (Fig. 1). To
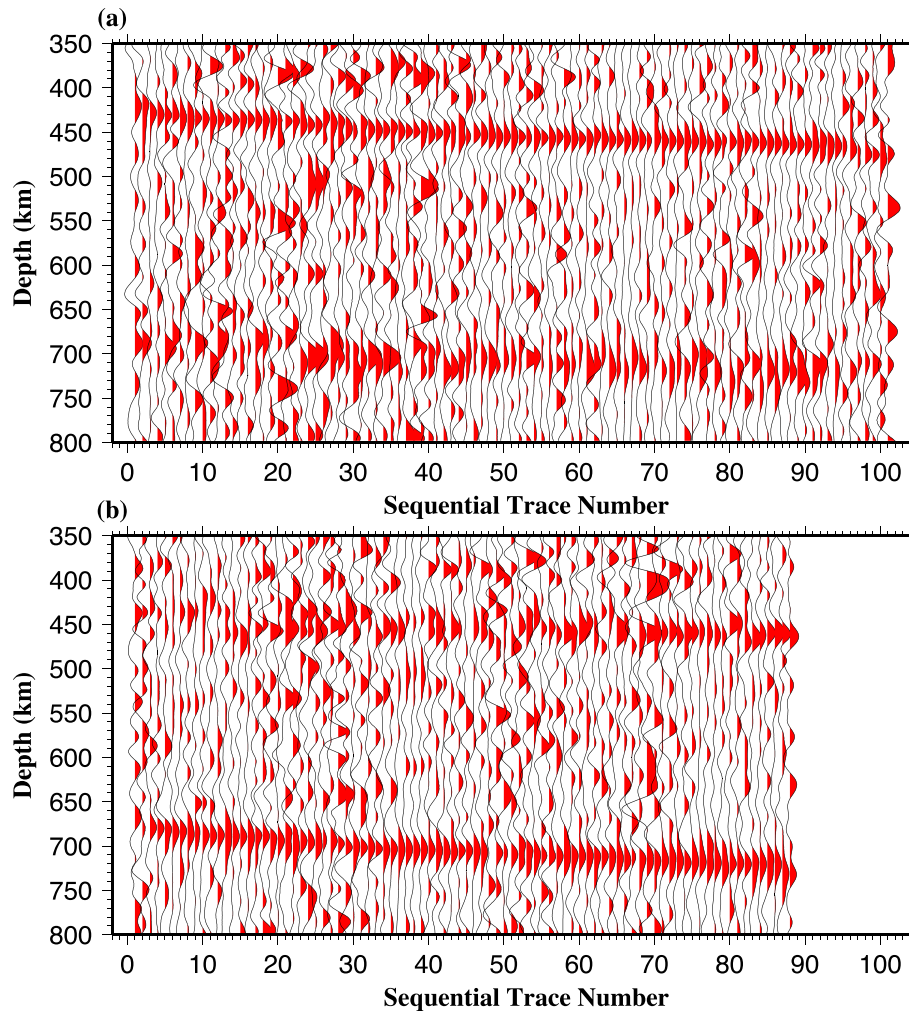
Figure 3. (a) Results of stacking all available normal moveout corrected RFs from 1° radius bins with a minimum of 10 high-quality RFs, plotted with sequentially increasing depth of the *d*410. (b) Same as (a) but for sequentially increasing depth of the *d*660.

ensure quality, bins with less than 10 RFs are not used in the study. RFs located within each of the bins are subjected to a bootstrap resampling procedure (Efron & Tibshirani 1986; Liu *et al.* 2003) with 50 iterations to calculate the mean and standard deviation of the discontinuity depths and the thickness of the MTZ. Visual checking of the stacked traces is conducted to reject unreliable peaks characterized by either weak arrivals or multiple similar-amplitude peaks. Note that because the 1-D IASP91 standard earth model is used for the moveout correction and time–depth conversion, the resulting discontinuity depths are apparent instead of true depths.
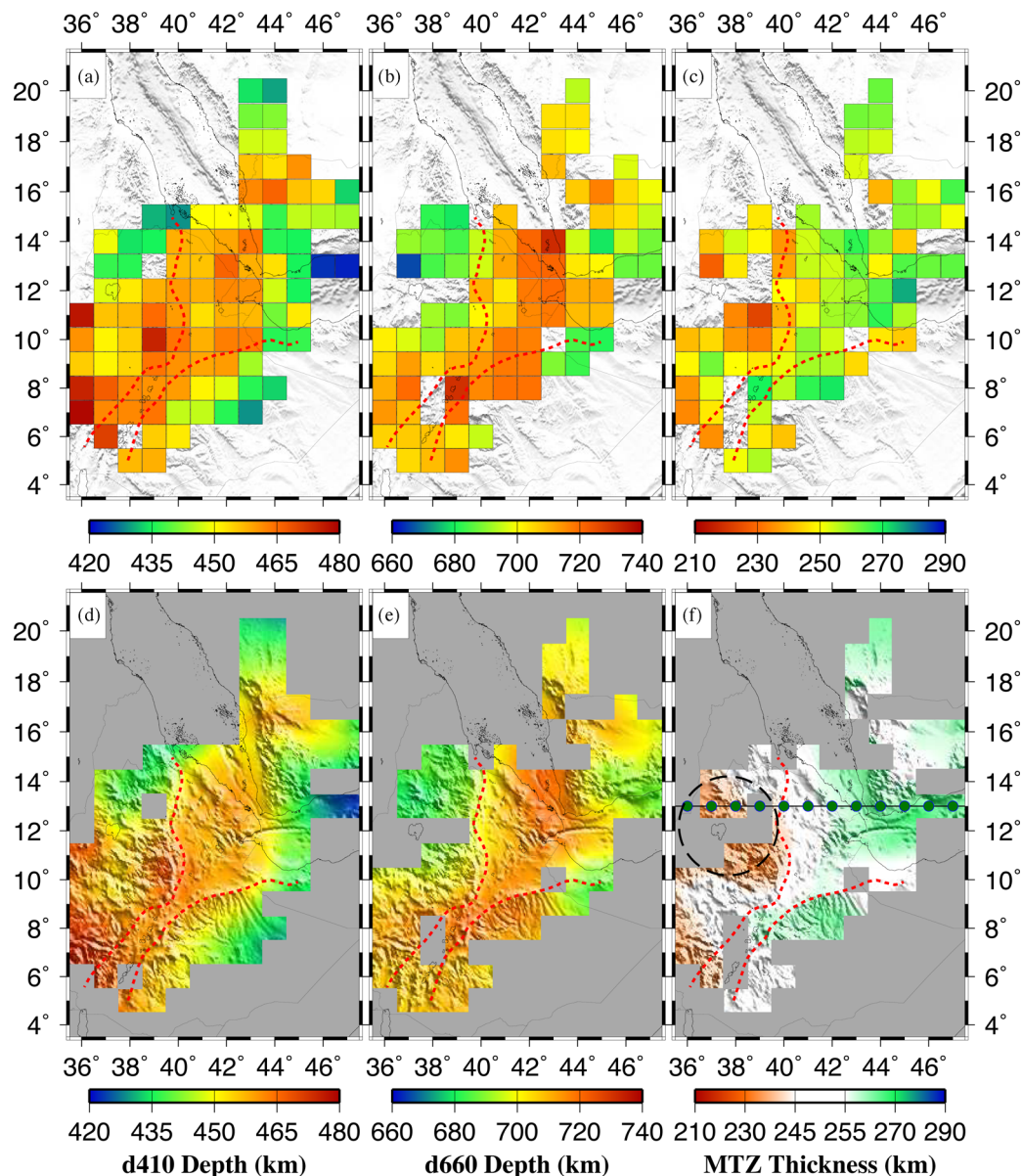
3 RESULTS

Among the 110 bins of radius 1° with clear *P*-to-*S* conversions from the *d*410 or *d*660 (or both), 101 possess clearly identifiable *d*410 peaks, 88 demonstrate reliable *d*660 arrivals and 79 exhibit arrivals from both discontinuities (Fig. 3). Profiles of the stacked traces along all latitudinal cross-sections are shown in Fig. S1, and all measurements may be found in Table S2. To improve the credibility of the stacking results, especially for bins with a low number of RFs along the edges of the study area (Fig. 1), we additionally stacked RFs in bins of radius 1.5° (Fig. S2) and 2.0° (Fig. S3). The resulting discontinuity depths and MTZ thicknesses (Fig. S4) are consistent

with those obtained using a radius of 1.0° (Fig. 4), albeit with a reduced horizontal resolution. Contrary to some of the previous studies which were unable to unambiguously detect the *d*410 (e.g. Nyblade *et al.* 2000; Benoit *et al.* 2006), robust *P*-to-*S* conversions from both the *d*410 and *d*660 are observed (Fig. 3) as a result of the greatly increased number of RFs employed in the stacking. Also revealed is a first-order parallelism between the MTZ discontinuities (Fig. 3), implying that variations in the apparent depths are mostly caused by velocity anomalies in the upper mantle which affect both discontinuities.

The apparent depths of both the *d*410 and *d*660 for all the bins (Fig. 4) exceed the global averages of 410 and 660 km, respectively, with respective averages of 451 ± 12 and 704 ± 13 km for the study area. Depths of the *d*410 are the shallowest at roughly 420 km beneath the Gulf of Aden on the eastern margin of the study area, while depressions of the *d*410 to over 470 km are observed beneath central Afar and the southeastern boundary of the western Ethiopian Plateau. The *d*660 is the shallowest at about 670 km beneath the northwestern extent of the western Plateau, and is the deepest at approximately 730 km beneath the southern Red Sea.

The entire study area is characterized by an apparent MTZ thickness of 252 ± 11 km, which is equivalent to the 250 km MTZ thickness in the IASP91 earth model. Three primary features in terms of the MTZ thickness distribution can be observed from Fig. 4.

Figure 4. Resulting depths for 1° radius bins determined using the IASP91 earth model for the *d*410 (a) & (d) and *d*660 (b) & (e) discontinuities as well as the thickness of the MTZ (c) & (f). Panels (a)–(c) demonstrate the discrete value for each bin, while (d)–(f) represent the smoothed topography. Thicknesses within 5 km of the global 250 km MTZ average have been whitened in panel F to emphasize the anomalously thickened or thinned regions of the MTZ. Green circles in (f) mark the bin centres for the E-W profile shown in Fig. 7), while the dashed circle roughly outlines the proposed plume stem beneath the Western Plateau.

First, the Afar Depression and northern MER are underlain by an MTZ possessing a normal thickness (within a tolerance of 5 km) as the consequence of an approximately 40–60 km depression for both discontinuities; second, an apparent thinning of the MTZ on the order of 20 km beneath the western Ethiopian Plateau is readily evident; and third, an apparent thickening in excess of about 15 km is visible beneath the junction of the southern Arabian plate, southern Red Sea and western Gulf of Aden. These three features are preserved in the instance where only bins with the best RF coverage (100 or more RFs per bin) are used (Fig. S5). They are also evident when all the RFs in each of the three regions are stacked (Fig. S6), as well as when RFs are grouped separately at 410 and 660 km (Fig. S7) instead of uniformly at 535 km. Spatial variations of MTZ thickness beneath the Afar are in general agreement with previous results (Nyblade *et al.* 2000; Cornwell *et al.* 2011; Thompson

et al. 2015), although our results for MTZ characteristics beneath the southern Red Sea, western Gulf of Aden and southern Arabian Plate are unique to the study area.

4 DISCUSSION

4.1 Apparent discontinuity depths and mantle velocity anomalies

The observed apparent depths of the MTZ discontinuities can, in principle, be converted into true depths by applying velocity corrections (e.g. Gao & Liu 2014b). Such corrections ultimately require reliably determined high-resolution *P*- and *S*-wave velocity models for both the upper mantle and MTZ in order to avoid artificially
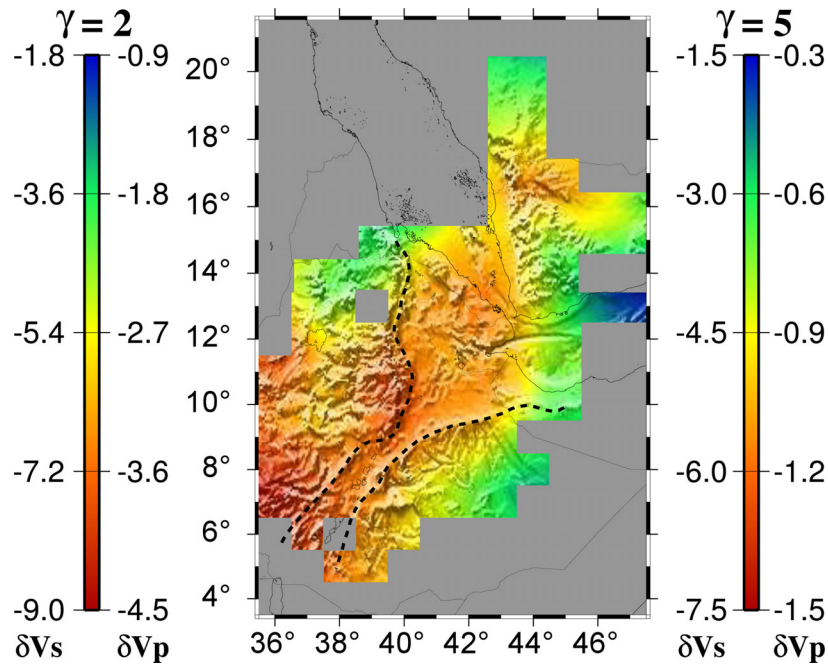
Figure 5. Required *P*- and *S*-wave velocity anomalies to correct the observed *d*410 depths beneath the study region to normal 410-km depth for *S*-to-*P* wave anomaly ratios (γ) of 2 and 5 relative to the IASP91 earth model.

introduced anomalies in the resulting 'true' depths and MTZ thickness (see fig. 3 of Mohamed *et al.* 2014, for a case when a fake plume is erroneously introduced by velocity corrections). Unfortunately, most existing body-wave tomography models for the study area (e.g. Bastow *et al.* 2008; Hammond *et al.* 2013; Civiero *et al.* 2015) do not possess sufficiently resolved velocity data beyond 400 km, and only a recent study (Thompson *et al.* 2015) was able to acquire *S*-wave relative velocity perturbations to depths exceeding 660 km. Furthermore, as argued in the following paragraph, if existing velocity models for the study area were used for making corrections, the depths would be inadequately corrected as a result of significant underestimation of the absolute velocity anomalies. Such underestimation is likely in regions such as the study area, which is characteristically dominated by some of the slowest mantle velocities worldwide (Bastow *et al.* 2008), because relative (i.e. mean-removed) rather than absolute traveltime residuals are pervasively used in body-wave tomography studies (Foulger *et al.* 2013).

The upper-mantle *P*- and *S*-wave velocity anomalies (averaged over the 0–410 km depth range) required to correct the discontinuities to their normal depths can be estimated using the observed apparent depths of the *d*410, following two assumptions: (1) the true (i.e. velocity corrected) depth of the *d*410 is 410 km, which is identical to the depth in the IASP91 earth model; and (2) the *P*- and *S*-wave relative velocity anomalies are related by a constant γ value beneath the entire study area. The γ factor, which is defined as $\gamma = dln(V_s)/dln(V_p)$, is variably dependent upon the presence of partial melt, attenuation structures and mineralogy of the upper mantle (Schmandt & Humphreys 2010). Resulting upper-mantle velocity anomalies shown in Fig. 5 were obtained using the relationship between the true and apparent depths and the velocity anomalies (eq. 8 in Gao & Liu 2014a). For γ = 2, the mean upper-mantle *P*- and *S*-wave anomalies required to correct the observed apparent *d*410 depths (which have a maximum value of about 470 km) to a depth of 410 km would reach −4.0 and −8.0 per cent, respectively, beneath the Ethiopian Plateau and Afar; the corresponding values are −1.4 and −7.0 per cent if a γ value of 5 is assumed.

None of the existing shear wave velocity models have such correspondingly high-velocity anomalies. For example, body-wave tomography for the Ethiopian upper mantle conducted by Bastow *et al.* (2008) reported *P*- and *S*-wave anomalies on the order of −1.5 and −2.5 per cent, respectively, and obtained positive velocity anomalies beneath the Ethiopian Plateau interiors. Therefore, applying existing velocity models for depth correction would lead to insufficiently corrected discontinuity depths. More importantly, because the velocity anomalies in the MTZ are usually not well resolved (Foulger *et al.* 2013), velocity corrections could lead to erroneous MTZ thicknesses (Mohamed *et al.* 2014).

4.2 Normal MTZ thicknesses beneath the Afar Depression and northern MER

Beneath the Afar Depression and the northern MER, both the *d*410 and *d*660 are depressed by 40–60 km and are parallel with each other, leading to a normal MTZ thickness. In the following, we explore the feasibility of three models that have the potential to fit the observed apparent depths of the discontinuities by utilizing the approach employed by Mohamed *et al.* (2014). The estimates below are based on Clapeyron slopes of +2.9 and −2.1 MPa K⁻¹ for the *d*410 and *d*660, respectively (Bina & Helffrich 1994), a velocity and temperature anomaly scaling factor of $\delta V_p/\delta T = 0.00048$ km s⁻¹ °C⁻¹ (Deal *et al.* 1999), and a γ factor of 3.0. While different assumptions naturally result in variably estimated magnitudes of MTZ discontinuity undulations, testing using various values suggests that the primary conclusions remain the same.

4.2.1 An active plume traversing the MTZ beneath Afar?

The existence of an active mantle plume beneath the Afar Depression has been proposed based on seismic tomography (Montelli *et al.* 2004; Civiero *et al.* 2015), MTZ imaging (Bastow *et al.* 2008; Cornwell *et al.* 2011; Thompson *et al.* 2015) and numerous
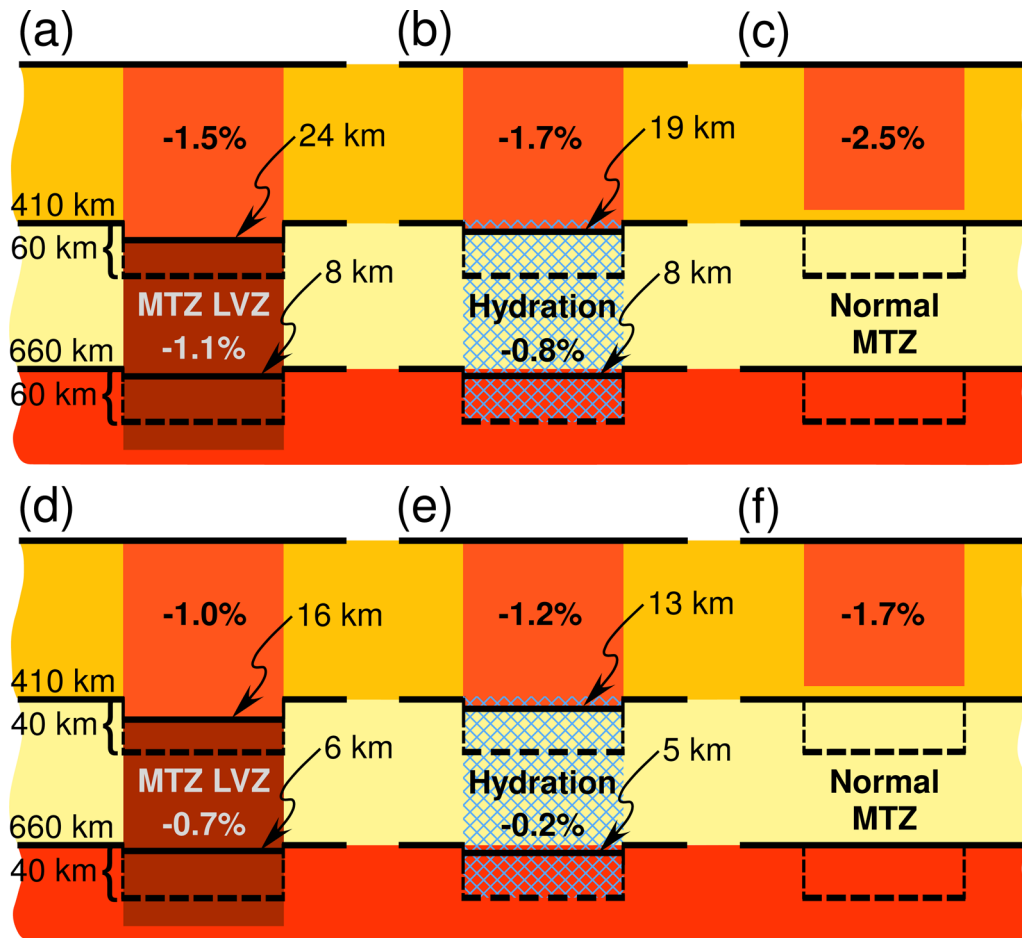
Figure 6. Hypothetical thermovelocity models put forth to justify the parallel apparent depression of MTZ discontinuities beneath the Afar Depression. (a)–(c) are for a 60 km and (d)–(f) are for a 40 km observed depression. Solid discontinuity lines indicate a real (due to thermal or hydration) shift of the discontinuity depth, whereas dashed lines indicate the final observed depth resulting from the combined effects of apparent uplift or depression due to velocity anomalies with thermal and/or hydrous influences. (a) and (d) An upper-mantle LVZ extending through the *d*410 and an MTZ LVZ extending into the lower mantle in a garnet dominated system. (b) and (e) An upper-mantle LVZ traversing the *d*410 with a hydrated MTZ. (c) and (f) An LVZ entirely constrained to the upper mantle inducing an equivalent apparent depression of both the *d*410 and *d*660. Note: the plots are not on scale.

geochemical studies (Hofmann *et al.* 1997; George *et al.* 1998; Kieffer *et al.* 2004; Furman *et al.* 2006). To construct a plume model (Fig. 6a) constituting a 60 km apparent depression of the *d*410, an upper mantle δV_p of −1.5 per cent transecting the *d*410 is needed. The low-velocity zone (LVZ), which extends from the surface to at least 440 km, induces a 36 km apparent depression of the *d*410. The velocity anomalies correspond to a 290 °C temperature increase if we consider the velocity–temperature relationship of Deal *et al.* (1999). The increased temperature leads to an additional 24 km depression of the *d*410 for a Clapeyron slope of +2.9 MPa K^{-1} (Bina & Helffrich 1994), achieving the 60 km apparent depression (Fig. 6a) beneath the Afar Depression and northern MER.

For an olivine-dominated phase transition across the *d*660, however, a low-velocity and high-temperature mantle plume traversing the *d*660 cannot produce a concurrent apparent depression of the *d*660 and maintain a normal MTZ thickness, primarily due to the opposite effect of a lower velocity, which increases the apparent depth of the *d*660, and the associated higher temperature, which uplifts the discontinuity (see Mohamed *et al.* 2014 for a quantitative model).

In order for the active plume model to produce a 60 km apparent depression of the *d*660, a majorite garnet to perovskite phase transition, which is characterized by a +1.3 MPa K^{-1} Clapeyron

slope (Hirose 2002), is required. Mineral physical experiments have demonstrated that such a phase transition is possible under high-temperature (exceeding 1800 °C) conditions (Hirose 2002). If we assume the same conditions for the *d*410 as stated above for a classical plume model, a normal MTZ can be achieved if we consider an apparent 52 km depression of the *d*660 as a consequence of an MTZ LVZ with an approximate $\delta V_p = -1.1$ per cent. This LVZ is coupled with a contemporaneous temperature increase of roughly 240 °C which would produce an additional 8 km downwarp along the *d*660 (Fig. 6a), resulting in the observed 60 km depression.

The temperature at the base of the MTZ has been estimated at roughly 1600 °C (Ito & Katsura 1989), and as such it is possible for the 240 °C temperature increase indicated above to reach the required 1800 °C for the garnet–perovskite transition. Our estimation of a 240 °C anomaly for a 60-km apparent depression model is similar to the prediction of Cornwell *et al.* (2011) for the MTZ beneath the northern MER, but not the Afar Depression wherein they suggested a normal olivine-dominated transition. This model requires a greater average low-velocity anomaly in the upper mantle than the MTZ (−1.5 versus −1.1 per cent). Such a difference in the amplitude of the average velocities can be explained by contributions from decompression melting in the upper mantle (e.g. Rychert *et al.* 2012). Note that, while the normal MTZ thicknesses observed

beneath the Afar Depression cannot preclude the existence of a mantle plume originated from the lower mantle, a specific combination of temperature, water content and velocity anomalies in the upper mantle and MTZ are required (Figs 6a and b). Such combinations may not be likely across the entire area, as discussed in detail in Section 4.2.3 below.

4.2.2 MTZ hydration

Another possibility to produce the apparently depressed MTZ discontinuities concomitant with a normal transition zone thickness involves a hydrated MTZ (Fig. 6b), wherein the presence of water serves both to thicken the MTZ through a simultaneous uplift and depression of the d410 and d660, respectively, and to decrease the seismic velocities in the MTZ. An instance of the hydrated 60 km depressed model (Fig. 6b) has an 8 km uplift of the d410 and the same amount of depression of the d660. In this instance, an upper-mantle LVZ consisting of a δV_p of approximately -1.70 per cent permeating the d410 will both apparently depress the d410 by 41 km and achieve a further 27 km depression through the effect of a concurrent 320 °C temperature increase. These apparent and true depressions along with the 8 km hydrous uplift will subsequently achieve a net depression of 60 km. Meanwhile, a 60 km depression of the d660 can be obtained by an apparent deepening of 52 km caused by the upper-mantle LVZ and an MTZ $\delta V_p = -0.8$ per cent, as well as the 8 km hydrous downwarp (Fig. 6b).

Thompson *et al.* (2015) proposed that the presence of a strong, continuous 520 km discontinuity (d520) as well as a negative arrival immediately above the d410 beneath Afar is suggestive of hydrous upwelling across the MTZ. Either feature is apparent on some of our stacked RFs (Figs S1–S3), but their limited spatial continuity prevents us from interpreting them as true features. Additionally, as demonstrated in Figs S1–S3, the amplitude of either feature reduces with increasing bin radius (and consequently the number of RFs participating in the stacking), a behaviour that is normally associated with the stacking of incoherent noise (see e.g. profile N11 in Figs S1–S3). In contrast, true arrivals such as those from the *P*410*s* and *P*660*s* are expected to be enhanced with the inclusion of additional RFs used for the stacking, as is observed (Figs S1–S3).

4.2.3 Upper-mantle low-velocity zone

The two models above require some specific combinations of velocity anomalies, temperature and/or quantities of water in the MTZ in order to explain the normal MTZ thickness across a large area, beneath which the observed apparent depths of the discontinuities vary spatially (Fig. 4). In reality, such a coincidence would be difficult to achieve. For instance, as shown in Fig. 6d, for a 40 km apparent depression of both discontinuities, the required magnitude of the upper-mantle LVZ reduces to -1.0 per cent, and that of the MTZ is now -0.7 per cent for the active lower-mantle plume model. For the MTZ hydration model, under the assumption that the undulation of the discontinuities due to hydration is 5 km, the required velocity anomalies become -1.2 per cent in the upper mantle and -0.2 per cent in the MTZ (Fig. 6e). Therefore, while the active plume or the hydrated MTZ model cannot be completely ruled out solely based on this study, we emphasize that such models are improbable given the specific conditions required for their generation.

The simplest and our favourite model to explain the parallelism of the apparently depressed MTZ discontinuities observed beneath the Afar Depression and northern MER involves an LVZ existing solely above but not traversing the d410. In order to achieve a parallel 60 km depression of the discontinuities, a mean *P*-wave velocity anomaly of -2.5 per cent in the 0–410 km depth range is required (Fig. 6c). Under this model, shallower apparent depths correspond to smaller upper-mantle velocity anomalies (e.g. Fig. 6f), and therefore, spatial variations of the apparent discontinuity depths simply reflect lateral variations of upper-mantle velocities.

The presence of such a broad, regionally anomalous LVZ is correlative with the concept of the heterogeneous hotter-than-normal upper mantle associated with the African Superswell (Kieffer *et al.* 2004) as the source of the Ethiopian LIP, as well as the likely consequent sublithospheric ponding of plume material remaining in the upper mantle (e.g. Dannberg & Sobolev 2015). Ongoing decompression melting owing to the thinning of rifted lithosphere (e.g. Rychert *et al.* 2012) may also contribute to the required upper-mantle low-velocity anomalies that produce the observed apparent depression of the MTZ discontinuities.

4.3 Anomalously thick MTZ beneath the southern Red Sea and adjacent areas

The amount of observed depression of the d660 beneath the southern Red Sea and the adjacent southern Arabian plate and western Gulf of Aden is about 15 km larger than that of the d410, leading to an MTZ that is ~15 km thicker than the global average of 250 km (Fig. 4). The thickening can also be observed when different bin radii and a greater number of RFs per bin are used (Figs S4 and S5). This area is the southward extension of the axial area of the Afro-Arabian Dome (AAD) in western Saudi Arabia, beneath which a 15 km thickening of the MTZ has also been observed (Mohamed *et al.* 2014). A total of seven possible models involving the effects of velocity (and associated temperature) anomalies, olivine- and garnet-dominated phase transitions and MTZ hydration have been discussed by Mohamed *et al.* (2014) to explain the apparent MTZ thickening beneath the AAD. The model that can best explain the 15 km MTZ thickening suggests that the axial area of the AAD is underlain by a combination of low seismic velocities in the upper mantle and hydrous minerals in the MTZ, probably accommodated by ancient subducted slabs (Stern 1994). Based on the arguments presented in Mohamed *et al.* (2014) and the fact that the area with thickened MTZ (Fig. 4f) is the southward extension of the AAD, we similarly interpret that hydrous minerals in the MTZ are likely responsible for the 15 km thickening of the MTZ beneath the southern Arabian Plate, southern Red Sea and the western Gulf of Aden. This hypothesis is consistent with recent findings from geochemical studies in northeastern China that delineated the capacity of the MTZ to absorb vast quantities of long-lived (i.e. $<10^9$ yr) supplies of water from the passage of ancient slabs (Kuritani *et al.* 2011).

4.4 A possible active plume stem beneath the Western Ethiopian Plateau

An apparent 20 km thinning of the MTZ is observable beneath the interior of the western Ethiopian Plateau between the latitudes of 10°N and 14°N (Figs 4f and 7). Because this region is on the edge of the study area and is sampled by a limited number of RFs, we use greater bin radii of 1.5° and 2.0° (Figs S2 and S3) to confirm the existence of MTZ thinning (Fig. S4). The observations in this area can be explained by an upper-mantle LVZ of lower magnitude than that beneath Afar overlying a positive thermal anomaly
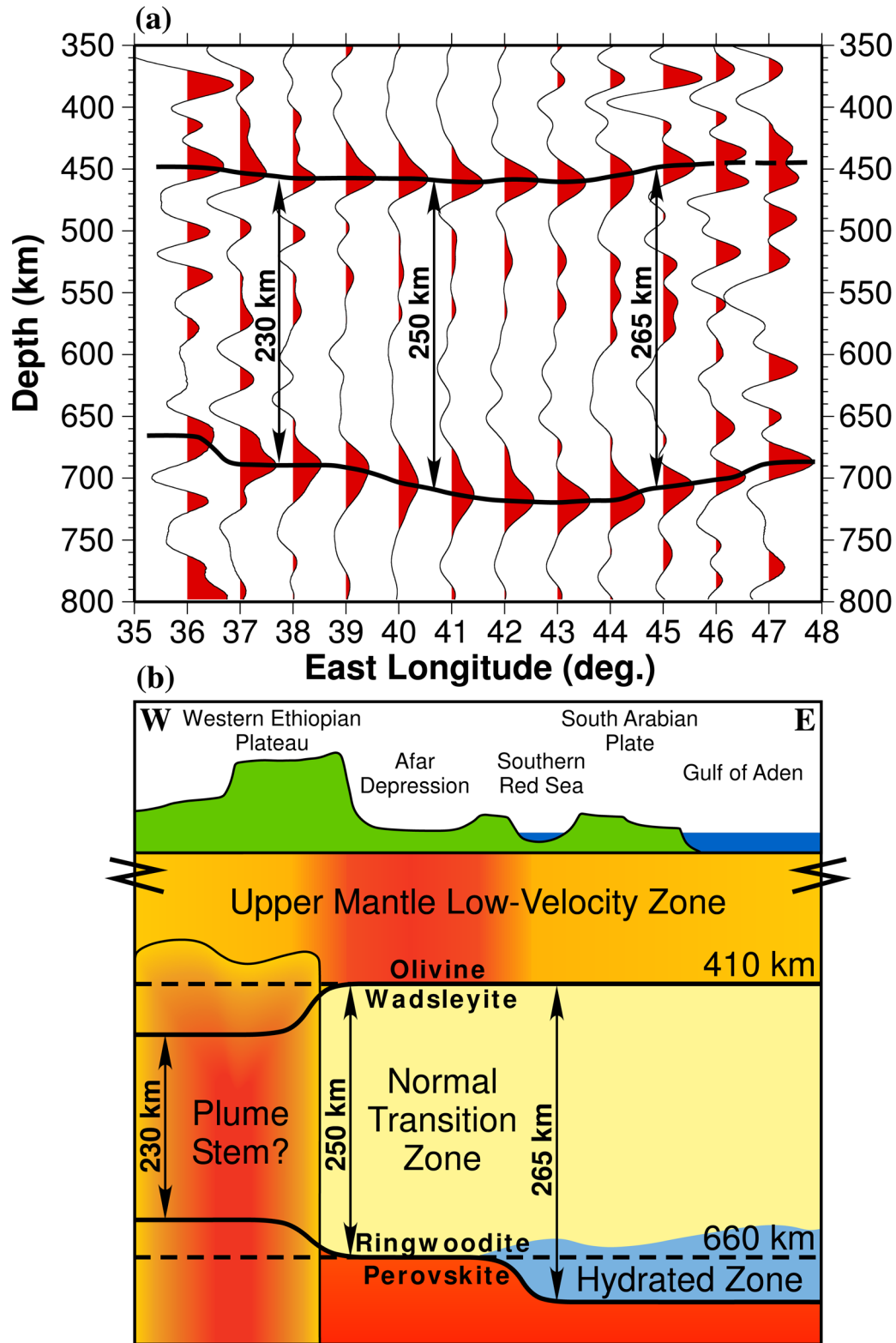
Figure 7. (a) Stacked RFs for bins of 2° radius along latitude 13°N with bold continuous lines tracing the observed apparent depths of the *d*410 and *d*660 for well-defined values and dashed line segments for unusable values. (b) Surface topography profile (top) and an MTZ discontinuity model (bottom) along latitude 13°N after a hypothetical velocity correction.

which traverses the whole transition zone (Fig. 7). The amount of apparent depression of both discontinuities corresponds to a constant −1 per cent V_p and a −2 per cent V_s anomaly and associated temperature increase extending from the surface to below the *d*660

(model D in Mohamed *et al.* 2014). If Clapeyron slope values of +2.9 and −2.1 MPa K^{-1} are considered for the *d*410 and *d*660, respectively (Bina & Helffrich 1994), then the 20 km thinning corresponds to a temperature anomaly of approximately 170 °C which

is well within the heat budget from a plume originating from the core–mantle boundary (Dannberg & Sobolev 2015). A plume stem beneath the western Plateau (Fig. 7) is consistent with the location of the suggested single-plume hypothesis of Ebinger & Sleep (1998) as well as the location of the oldest shield volcano within the Western Plateau which Kieffer *et al.* (2004) attributed to an Oligocene plume. Low velocities beneath the Western Plateau detected at depths of >400 km by Bastow *et al.* (2008) and Civiero *et al.* (2015) are also consistent with our findings.

Numerical models tested by Dannberg & Sobolev (2015) show that it is possible for sufficiently large, lower-mantle-origin plumes characterized by the entrainment of high-viscosity, eclogitic oceanic crust to demonstrate a plume tail with a diameter in excess of 500 km and a longevity of 200 Ma in the MTZ. These features of a low-buoyancy plume stem may account for the broad region of 20-km thinning of the MTZ beneath the Western Plateau (Fig. 7). We must note, however, that without appropriate velocity corrections, we cannot resolve whether this apparent thinning is the result of such a plume or possibly a combination of low- and high-velocity material above the $d410$ and within the MTZ, respectively, as the latter would serve to induce the observed uplift of the $d660$. Additional data acquired in western Ethiopia away from the rift system would serve to approach this subject more appropriately.

5 CONCLUSIONS

This study has utilized an unprecedented quantity of over 14 500 high-quality radial RFs recorded over the past two decades by stations belonging to a compilation of 12 independent networks within the Afar Depression and adjacent regions to image the apparent depths of the 410 and 660 km discontinuities. Contrary to some of the previous studies utilizing a lower quantity of RFs, we have observed robust *P*-to-*S* conversions for both the $d410$ and $d660$ throughout the study area. The apparent depths of both discontinuities regionally exceed the global averages and are generally parallel to each other, and thus indicate a broad upper-mantle low-velocity anomaly stretching beneath the entirety of the study area. Parallel MTZ discontinuities and normal transition zone thickness beneath the Afar Depression indicate the absence of thermal anomalies deeper than 410 km, and an ∼20 km thinning of the MTZ beneath the Western Ethiopian Plateau may suggest focused upwelling associated with an active mantle plume stem originating from the lower mantle. Thickening of the MTZ of about 15 km in magnitude beneath the joint area of the southern Arabian Plate, southern Red Sea and western Gulf of Aden suggests substantial MTZ hydration, most likely as the result of Precambrian subduction processes.

ACKNOWLEDGEMENTS

REFERENCES

Ammon, C.J., 1991. The isolation of receiver effects from teleseismic *P*-waveforms, *Bull. seism. Soc. Am.,* **81,** 2504–2510.

Bastow, I.D., Nyblade, A.A., Stuart, G.W., Rooney, T.O. & Benoit, M.H., 2008. Upper mantle seismic structure beneath the Ethiopian hot spot: rift-ing at the edge of the African low-velocity anomaly, *Geochem. Geophys. Geosyst.,* **9**(12), Q12022, doi:10.1029/2008GC002107.

Behn, M.D., Conrad, C.P. & Silver, P.G., 2004. Detection of upper mantle flow associated with the African Superplume, *Earth planet. Sci. Lett.,* **224,** 259–274.

Benoit, M.H., Nyblade, A.A., Owens, T.J. & Stuart, G., 2006. Mantle transition zone structure and upper mantle S velocity variations beneath Ethiopia: evidence for a broad, deep-seated thermal anomaly, *Geochem. Geophys. Geosyst.,* **7**(11), Q11013, doi:10.1029/2006GC001398.

Bina, C.R. & Helffrich, G., 1994. Phase transition Clapeyron slopes and transition zone seismic discontinuity topography, *J. geophys. Res.,* **99,** 15 853–15 860.

Bolfan-Casanova, N., Keppler, H. & Rubie, D.C., 2000. Water partitioning between nominally anhydrous minerals in the $MgO-SiO_2-H_2O$ system up to 24 GPa: implications for the distribution of water in the Earth's mantle, *Earth planet. Sci. Lett.,* **182,** 209–221.

Chevrot, S., Vinnik, L. & Montagner, J.-P., 1999. Global-scale analysis of the mantle Pds phases, *J. geophys. Res.,* **104**(B9), 20 203–20 219.

Civiero, C. *et al.*, 2015. Multiple mantle upwellings in the transition zone beneath the northeast East-African Rift system from relative P-wave travel-time tomography, *Geochem. Geophys. Geosyst.,* **16,** 2949–2968.

Coffin, M.F. & Eldholm, O., 1994. Large igneous provinces: crustal structure, dimensions, and external consequences, *Rev. Geophys.,* **32**(1), 1–36.

Cornwell, D.G., Hetenyi, G. & Blanchard, T.D., 2011. Mantle transition zone variations beneath the Ethiopian Rift and Afar: chemical heterogeneity within a hot mantle?, *Geophys. Res. Lett.,* **38,** L16308, doi:10.1029/2011GL047575.

Dannberg, J. & Sobolev, S.V., 2015. Low-buoyancy thermochemical plumes resolve controversy of classical mantle plume concept, *Nature Commun.,* **6,** doi:10.1038/ncomms7960.

Deal, M.M., Nolet, G. & van der Hilst, R.D., 1999. Slab temperature and thickness from seismic tomography: 1. Method and application to Tonga, *J. geophys. Res.,* **38,** 28 789–28 802.

Ebinger, C.J. & Sleep, N.H., 1998. Cenozoic magmatism throughout east Africa resulting from impact of a single plume, *Nature,* **395,** 788–791.

Ebinger, C.J., Yemane, T., Woldegabriel, G., Aronson, J.L. & Walter, R.C., 1993. Late Eocene-Recent volcanism and faulting in the southern main Ethiopian rift, *J. geol. Soc. Lond.,* **150,** 99–108.

Efron, B. & Tibshirani, R., 1986. Bootstrap methods for standard errors, confidence intervals, and other measures of statistical accuracy, *Stat. Sci.,* **1,** 54–77.

Ferguson, D.J. *et al.*, 2013. Melting during late-stage rifting in Afar is hot and deep, *Nature,* **499,** 70–73.

Foulger, G.R. *et al.*, 2013. Caveats on tomographic images, *Terra Nova,* **25,** 259–281.

Furman, T., Bryce, J., Rooney, T., Hanan, B., Yirgu, G. & Ayalew, D., 2006. Heads and tails: 30 million years of the Afar plume, in *The Structure and Evolution of the East African Rift System in the Afar Volcanic Province,* pp. 95–119, eds Yirgu, G., Ebinger, C.J. & Maguire, P.K.H., *Geol. Soc. London Spec. Pub.,* **259,** doi:10.1144/GSL.SP.2006.259.0.1.09.

Gao, S.S. & Liu, K.H., 2014a. Imaging mantle discontinuities using multiply-reflected *P*-to-*S* conversions, *Earth planet. Sci. Lett.,* **402,** 99–106.

Gao, S.S. & Liu, K.H., 2014b. Mantle transition zone discontinuities beneath the contiguous United States, *J. geophys. Res.,* **119,** 6452–6468.

George, R., Rogers, N. & Kelley, S., 1998. Earliest magmatism in Ethiopia: evidence for two mantle plumes in one flood basalt province, *Geology,* **26,** 923–926.

Hammond, J.O.S. *et al.*, 2013. Mantle upwelling and initiation of rift segmentation beneath the Afar Depression, *Geology,* **41,** 635–638.

Hansen, S.E. & Nyblade, A.A., 2013. The deep seismic structure of the Ethiopia/Afar hotspot and the African superplume, *Geophys. J. Int.,* **194,** 118–124.

Hirose, K., 2002. Phase transitions in pyrolitic mantle around 670-km depth: implications for upwelling of plumes from the lower mantle, *J. geophys. Res.,* **107,** doi:10.1029/2001JB000597.

Hofmann, C., Courtillot, V., Féraud, G., Rochette, P., Yirgu, G., Ketefo, E. & Pik, R., 1997. Timing of the Ethiopian flood basalt event

and implications for plume birth and global change, *Nature,* **389,** 838–841.

Ito, E. & Katsura, T., 1989. A temperature profile of the mantle transition zone, *Geophys. Res. Lett.,* **16,** 425–428.

Jellinek, A.M. & Manga, M., 2004. Links between long-lived hot spots, mantle plumes, D″, and plate tectonics, *Rev. Geophys.,* **42,** RG3002, doi:10.1029/2003RG000144.

Kieffer, B. *et al.*, 2004. Flood and shield basalts from Ethiopia: magmas from the African superswell, *J. Petrol.,* **45,** 793–834.

Kuritani, T., Ohtani, E. & Kimura, J.-I., 2011. Intensive hydration of the mantle transition zone beneath China caused by ancient slab stagnation, *Nature Geosci.,* **4,** 713–716.

Litasov, K.D., Ohtani, E., Sano, A., Suzuki, A. & Funakoshi, K., 2005. Wet subduction versus cold subduction, *Geophys. Res. Lett.,* **32,** L13312, doi:10.1029/2005GL022921.

Lithgow-Bertelloni, C. & and Silver, P.G., 1998. Dynamic topography, plate driving forces and the African superswell, *Nature,* **395,** 269–272.

Liu, K.H., Gao, S.S., Silver, P.G. & Zhang, Y., 2003. Mantle layering across central South America, *J. geophys. Res.,* **108,** 2510, doi:10.1029/2002JB002208.

Mohamed, A.A., Gao, S.S., Elsheikh, A.A., Liu, K.H., Yu, Y. & Fat-Helbary, R.E., 2014. Seismic imaging of mantle transition zone discontinuities beneath the northern Red Sea and adjacent areas, *Geophys. J. Int.,* **199,** 648–657.

Montelli, R., Nolet, G., Dahlen, F.A., Masters, G., Engdahl, E.R. & Hung, S.-H., 2004. Finite-frequency tomography reveals a variety of plumes in the mantle, *Science,* **303,** 338–343.

Nyblade, A.A., Knox, R.P. & Gurrola, H., 2000. Mantle transition zone thickness beneath Afar: implications for the origin of the Afar hotspot, *Geophys. J. Int.,* **142,** 615–619.

Ohtani, E., Litasov, K., Hosoya, T., Kubo, T. & Kondo, T., 2004. Water transport into the deep mantle and formation of a hydrous transition zone, *Phys. Earth planet. Inter.,* **143–144,** 255–269.

Reed, C.A., Almadani, S., Gao, S.S., Elsheikh, A.A., Cherie, S., Abdelsalam, M.G., Thurmond, A.K. & Liu, K.H., 2014. Receiver function constraints on crustal seismic velocities and partial melting beneath the Red Sea rift and adjacent regions, Afar Depression, *J. geophys. Res.,* **119**(3), 2138–2152.

Ringwood, A.E., 1975. *Composition and Petrology of the Earth's Mantle,* 1st edn, p. 672, McGraw-Hill.

Rooney, T.O., Herzberg, C. & Bastow, I.D., 2012. Elevated mantle temperature beneath East Africa, *Geology,* **40,** 27–30.

Rychert, C.A. *et al.*, 2012. Volcanism in the Afar Rift sustained by decompression melting with minimal plume influence, *Nature Geosci,,* **5,** 406–409.

Schmandt, B. & Humphreys, E., 2010. Seismic heterogeneity and small-scale convection in the southern California upper mantle, *Geochem. Geophys. Geosyst.,* **11,** Q05004, doi:10.1029/2010GC003042.

Stern, R.J., 1994. Arc-assembly and continental collision in the Neoproterozoic African orogen: implications for the consolidation of Gondwanaland, *Annu. Rev. Earth Planet. Sci.,* **22,** 319–351.

Tauzin, B. & Ricard, Y., 2014. Seismically deduced thermodynamics phase diagrams for the mantle transition zone, *Earth planet. Sci. Lett.,* **401,** 337–346.

Tauzin, B., Debayle, E. & Wittlinger, G., 2008. The mantle transition zone as seen by global Pds phases: no clear evidence for a thin transition zone beneath hotspots, *J. geophys. Res.,* **113,** B08309, doi:10.1029/2007JB005364.

Thompson, D.A., Hammond, J.O.S., Kendall, J-M., Stuart, G.W., Helffrich, G., Keir, D., Ayele, A. & Goitom, B., 2015. Hydrous upwelling across the mantle transition zone beneath the Afar Triple Junction, *Geochem. Geophys. Geosyst.,* **16,** 834–846.

SUPPORTING INFORMATION

Additional Supporting Information may be found in the online version of this paper:

Table S1. Breakdown of the 12 individual seismic networks used in this study as well as the total number of stations used from each network, the number of receiver functions obtained, and the period of operation.

Table S2. Results of bootstrap resampling averaging of picked MTZ discontinuity depths for all $1°$ radius circular bins with 10 or more high-quality receiver functions.

Figure S1. Stacked latitudinal traces of time-series receiver functions (RFs) converted into depth-series RFs using the IASP91 Earth model velocities. Dashed lines represent the standard error of the binned trace amplitude from a bootstrap sample of 50 traces. Black dots with associated standard error mark the depth value obtained from bootstrap resampling of 50 resampled traces for each $1°$ radius bin.

Figure S2. Same as Fig. S1, but for stacked latitudinal traces of time-series RFs for bins of $1.5°$ radius.

Figure S3. Same as Fig. S1, but for stacked latitudinal traces of time-series RFs for bins of $2.0°$ radius.

Figure S4. Resulting apparent depths for bins of $1.5°$ radius (panels a through c) and $2.0°$ radius (panels d through f) for the $d410$ (a & d) and $d660$ (b & e) and for the MTZ thickness (c & f) with a minimum hit count of 10 RFs per bin. Dashed circles in panels (c) and (f) mark the proposed location of the plume stem beneath the Western Plateau from Fig. 4. Green dots in (f) mark the bin centres of the profile used in Fig. 7(a).

Figure S5. Resulting apparent depths in $1°$ radius bins with minimum RF counts of 100 (panels a through c) and 200 (panels d through f) for the $d410$ (a & c), $d660$ (b & e), and the MTZ thickness (c & f). Dashed circles in panels (c) and (f) mark the proposed location of the plume stem beneath the Western Plateau from Fig. 4.

Figure S6. RF Stacks for the Western Plateau (left, 1474 RFs), Afar Depression (centre, 7159 RFs), and Gulf of Aden (right, 1260 RFs) binned RFs. The top panel depicts the summed RF stack of all RFs from each respective area, while the three bottom panels demonstrate the binned stacks from each region sorted according to increasing apparent depth of the $d410$ for bins of radius $1.0°$, $1.5°$, and $2.0°$.

Figure S7. Resulting apparent depths in $1°$ radius bins for (a) the $d410$ using piercing points computed for 410 km and (b) the $d660$ using piercing points computed for 660 km with a minimum hit count of 10 RFs per bin. (c) MTZ apparent thickness using the arithmetic difference between the values from panels (a) and (b). Dashed circle in (c) indicates the proposed location of the plume stem from Fig. 4.

(http://gji.oxfordjournals.org/lookup/suppl/doi:10.1093/gji/ggw116/-/DC1)

Please note: Oxford University Press is not responsible for the content or functionality of any supporting materials supplied by the authors. Any queries (other than missing material) should be directed to the corresponding author for the paper.